ALMA Survey of Orion Planck Galactic Cold Clumps (ALMASOP): Deriving Inclination Angle and Velocity of the Protostellar Jets from Their SiO Knots

Kai-Syun Jhan[1,2] , Chin-Fei Lee[2,1] , Doug Johnstone[3,4] , Tie Liu[5] , Sheng-Yuan Liu[2] , Naomi Hirano[2] ,
Ken'ichi Tatematsu[6,7] , Somnath Dutta[2] , Anthony Moraghan[2] , Hsien Shang[2] , Jeong-Eun Lee[8] , Shanghuo Li[9] ,
Chun-Fan Liu[2] , Shih-Ying Hsu[2,10] , Woojin Kwon[11,12] , Dipen Sahu[2] , Xun-Chuan Liu[5] , Kee-Tae Kim[9,13] , Qiuyi Luo[5],
Sheng-Li Qin[14] , Patricio Sanhueza[7,15] , Leonardo Bronfman[16] , Zhang Qizhou[17] , David Eden[18] ,
Alessio Traficante[19] , and Chang Won Lee[9,13]
ALMASOP Team

[1] Graduate Institute of Astronomy and Astrophysics, National Taiwan University, No. 1, Sec. 4, Roosevelt Road, Taipei 10617, Taiwan; ksjhan@asiaa.sinica.edu.tw, cflee@asiaa.sinica.edu.tw
[2] Academia Sinica Institute of Astronomy and Astrophysics, No. 1, Sec. 4, Roosevelt Road, Taipei 10617, Taiwan
[3] National Research Council of Canada, Herzberg, Astronomy and Astrophysics Research Centre, 5071 West Saanich Road, V9E 2E7 Victoria (BC), Canada
[4] Department of Physics and Astronomy, University of Victoria, Victoria, BC V8P 5C2, Canada
[5] Shanghai Astronomical Observatory, Chinese Academy of Sciences, 80 Nandan Road, Shanghai 200030, People's Republic of China
[6] Nobeyama Radio Observatory, National Astronomical Observatory of Japan, National Institutes of Natural Sciences, 462-2 Nobeyama, Minamimaki, Minamisaku, Nagano 384-1305, Japan
[7] Department of Astronomical Science, SOKENDAI (The Graduate University for Advanced Studies), 2-21-1 Osawa, Mitaka, Tokyo 181-8588, Japan
[8] School of Space Research, Kyung Hee University, Yongin-Si, Gyeonggi-Do 17104, Republic of Korea
[9] Korea Astronomy and Space Science Institute (KASI), 776 Daedeokdae-ro, Yuseong-gu, Daejeon 34055, Republic of Korea
[10] Graduate Institute of Physics, National Taiwan University, No. 1, Sec. 4, Roosevelt Road, Taipei 10617, Taiwan
[11] Department of Earth Science Education, Seoul National University, 1 Gwanak-ro, Gwanak-gu, Seoul 08826, Republic of Korea
[12] SNU Astronomy Research Center, Seoul National University, 1 Gwanak-ro, Gwanak-gu, Seoul 08826, Republic of Korea
[13] University of Science and Technology, Korea (UST), 217 Gajeong-ro, Yuseong-gu, Daejeon 34113, Republic of Korea
[14] Department of Astronomy, Yunnan University, and Key Laboratory of Particle Astrophysics of Yunnan Province, Kunming, 650091, People's Republic of China
[15] National Astronomical Observatory of Japan, National Institutes of Natural Sciences, 2-21-1 Osawa, Mitaka, Tokyo 181-8588, Japan
[16] Departamento de Astronomía, Universidad de Chile, Casilla 36-D, Santiago, Chile
[17] Center for Astrophysics—Harvard & Smithsonian, 60 Garden Street, Cambridge, MA 02138, USA
[18] Armagh Observatory and Planetarium, College Hill, Armagh, BT61 9DB, UK
[19] IAPS-INAF, via Fosso del Cavaliere 100, I-00133, Rome, Italy

Abstract

We have selected six sources (G209.55–19.68S2, G205.46–14.56S1_A, G203.21–11.20W2, G191.90–11.21S, G205.46–14.56S3, and G206.93–16.61W2) from the Atacama Large Millimeter/submillimeter Array Survey of Orion Planck Galactic Cold Clumps (ALMASOP), in which these sources have been mapped in the CO ($J = 2-1$), SiO ($J = 5-4$), and $C^{18}O$ ($J = 2-1$) lines. These sources have high-velocity SiO jets surrounded by low-velocity CO outflows. The SiO jets consist of a chain of knots. These knots have been thought to be produced by semiperiodic variations in jet velocity. Therefore, we adopt a shock-forming model, which uses such variations to estimate the inclination angle and velocity of the jets. We also derive the inclination angle of the CO outflows using the wide-angle wind-driven shell model and find it to be broadly consistent with that of the associated SiO jets. In addition, we apply this shock-forming model to another three protostellar sources with SiO jets in the literature— HH 211, HH 212, and L1448C(N)—and find that their inclination angle and jet velocity are consistent with those previously estimated from proper-motion and radial-velocity studies.

Unified Astronomy Thesaurus concepts: Shocks (2086); Star formation (1569); Stellar jets (1607); Stellar winds (1636); Young stellar objects (1834)

1. Introduction

Protostellar jets are important components in star formation. They are launched from the innermost parts of accretion disks and carry away angular momentum, allowing the disk material to fall onto the protostars (Frank et al. 2014; Lee 2020). However, the location where this launching process occurs (<1 au) is too close to the protostar to be spatially resolved with current observational facilities. Therefore, protostellar jet properties, such as velocity and mass-loss rate, are used to constrain the launching

mechanism. However, it requires multiepoch observations with enough spatial and velocity resolution over several years to measure the jet proper motion in order to derive the jet velocity. In addition, the inclination angle of the jet, which is also needed to derive the jet velocity, cannot be measured directly. Here we employ a novel method to constrain both the inclination angle and the jet velocity, requiring only one epoch of observation.

Now, with the Atacama Large Millimeter/submillimeter Array (ALMA), protostellar jets can be resolved with sufficient resolution. They have knotty (shock) structures traced by shock tracers, e.g., SiO (Gueth et al. 1998; Hirano et al. 2006; Palau et al. 2006; Codella et al. 2007; Lee et al. 2007; Podio et al. 2021), H_2 (McCaughrean et al. 1994; Zinnecker et al. 1998), and SO (Lee et al. 2007, 2010; Podio et al. 2021). These knots have been

thought to trace the (internal) shocks produced by semiperiodic variations in jet velocity at the launching points (see, e.g., Raga et al. 1990; Stone & Norman 1993; Suttner et al. 1997; Lee et al. 2001). Therefore, we adopt the shock-forming model (Raga et al. 1990; Lee & Sahai 2004), which uses such variations, to derive the inclination angle and jet velocity from the knots in the jets. This model has also been used to account for the lack of SiO knotty shocks near the central source in HH 211 (Jhan & Lee 2021).

In this Letter, we report the detections of protostellar jets and outflows in the SiO ($J = 5 - 4$) and CO ($J = 2-1$) transitions with ALMA in six Class 0 and I sources, G209.55–19.68S2 (HOPS 10), G205.46–14.56S1_A (HOPS 358), G203.21–11.20W2, G191.90–11.21S, G205.46–14.56S3 (HOPS 315), and G206.93–16.61W2 (HOPS 399) (hereafter G209, G205, G203, G191, G205S3, and G206 respectively), and test the shock-forming model. We present the observations in Section 2. In Section 3, we present the results of the jets and use the shock-forming model to estimate the inclination angle and velocity of the jets. We also present the results of the outflows and use the wind-driven shell model (Lee et al. 2000) to derive the inclination angle of the outflows. In Section 4, we compare the inclination angles derived from both models, apply the shock-forming model to other sources reported in the literature, and then discuss jet and outflow properties and the jet knot timescales. We summarize our conclusions in Section 5.

2. Observations

Observations toward the G209, G205, G203, G191, G205S3, and G206 systems were obtained with ALMA (ID: 2018.1.00302.S; PI: Tie Liu). The data are part of the ALMA Survey of Orion Planck Galactic Cold Clumps (ALMASOP) project (Dutta et al. 2020; Hsu et al. 2020; Sahu et al. 2021), in which only these six targeted sources were seen with clear periodic knotty structures. We have mapped these targeted sources in $C^{18}O$ $J = 2-1$ (219.560 GHz) to determine their systemic velocities and mapped their outflows and jets in the CO $J = 2-1$ (230.538 GHz) and SiO $J = 5-4$ (217.105 GHz) lines. More details on the calibration and the line observations can be seen in Dutta et al. (2020, 2022). Here we only summarize the important parameters for the three lines. The CASA 5.4 package was used to image the data. These sources were observed with three different configurations, resulting in three different data sets (TM1, TM2, and ACA). After combining these data sets, we used the TCLEAN task with a robust weighting factor of 0.5 to generate various line-intensity maps with a velocity resolution of $\sim 1.6\,\mathrm{km\,s^{-1}}$, without primary beam correction. The synthesized beam has a size of $\sim 0.''35 \times 0.''31$ for CO, $\sim 0.''40 \times 0.''32$ for SiO, and $\sim 0.''43 \times 0.''31$ for $C^{18}O$. The resulting CO, SiO, and $C^{18}O$ channel maps have a noise level of ~ 2.2, 2.0, and 2.7 mJy beam^{-1}, respectively.

3. Results and Models

In each source, the systemic velocity V_{sys} is assumed to be the velocity at the peak emission of the $C^{18}O$ position–velocity (PV) structure cut perpendicular to the jet axis going through the sources' center. It is found to be 8.0 ± 0.8, 9.6 ± 0.8, 9.6 ± 0.8, 10.4 ± 0.8, 9.9 ± 0.8, and $8.8 \pm 0.8\,\mathrm{km\,s^{-1}}$ for G209, G205, G203, G191, G205S3, and G206, respectively (see Figure A1 in Appendix A and Figure 4 in Dutta et al.

2022). Throughout this paper, the velocity of the jet or outflow is the velocity offset relative to the systemic value.

3.1. SiO Jets and the Shock-forming Model

Figures 1(a) to (f) show the SiO maps of our six sources. For all targets, the SiO emission (contours) is highly collimated and consists of a chain of knots tracing the jets. These jets can also be traced by high-velocity CO gas, as shown in color images. The underlying jets could be continuous structures, and SiO mainly traces the internal shocks, where the density is high. Therefore, throughout this Letter, the SiO jet means a jet-like structure consisting of a chain of high-density shocked regions detected in SiO. Notice that four of the jets (G209, G205, G203, and G191) happen to be monopolar jets in both SiO and CO and are seen only on the redshifted side, and the other two jets (G205S3 and G206) are bipolar.

Interestingly, there is no SiO emission between the central sources and their first (closest) knots in four of the jets. This phenomenon has been observed in other sources, e.g., HH 211 (Jhan & Lee 2021), and can be explained by a shock-forming model. In this model, the sources eject jet material with a periodic variation in the jet velocity to form internal shocks (knots, Raga et al. 1990; Stone & Norman 1993; Suttner et al. 1997; Lee & Sahai 2004), producing SiO in the gas phase and thus the SiO emission (Schilke et al. 1997). However, an internal shock does not form immediately near the source because it takes time (or distance) for the fast material to catch up with the slow material, as shown in Figure 1(g).

In the model, the jet is assumed to have the following velocity,

$$V = V_{\mathrm{j}} - \frac{\Delta V}{2} \sin\left(\frac{2\pi t}{P}\right), \quad (1)$$

where V is the jet velocity at a certain position, V_{j} is the mean jet velocity, ΔV is the amplitude of the velocity variation, t is the time, and P is the period of the variation (Raga et al. 1990; Lee & Sahai 2004).

An internal shock forms when the fastest material with $V_{\mathrm{j}} + \Delta V/2$ catches up (and collides) with the slowest material having V_{j}–$\Delta V/2$ (see Figure 1(g)). The distance to catch up is given by the following:

$$D = V_{\mathrm{j}} \frac{V_{\mathrm{j}}}{\Delta V/(P/\pi)}, \quad (2)$$

where the value of $\left(\frac{V_{\mathrm{j}}}{\Delta V/(P/\pi)}\right)$ is the time to catch up (Raga et al. 1990; Lee & Sahai 2004). After forming, the shocks are moving at the mean jet velocity (V_{j}). Therefore, the interval of the knots (ΔD) is given as

$$\Delta D = P V_{\mathrm{j}}. \quad (3)$$

Combining Equations (2) and (3) and rearranging, we obtain

$$V_{\mathrm{j}} = \pi \frac{D}{\Delta D} \Delta V. \quad (4)$$

In addition, we assume no energy dissipation so that the thermal energy produced by the shocks would be totally transferred sideways into the sideways ejection. Thus, the sideways-ejection velocity is equal to ΔV. Then, the observed radial sideways-ejection velocity (ΔV_{obs}) and the observed
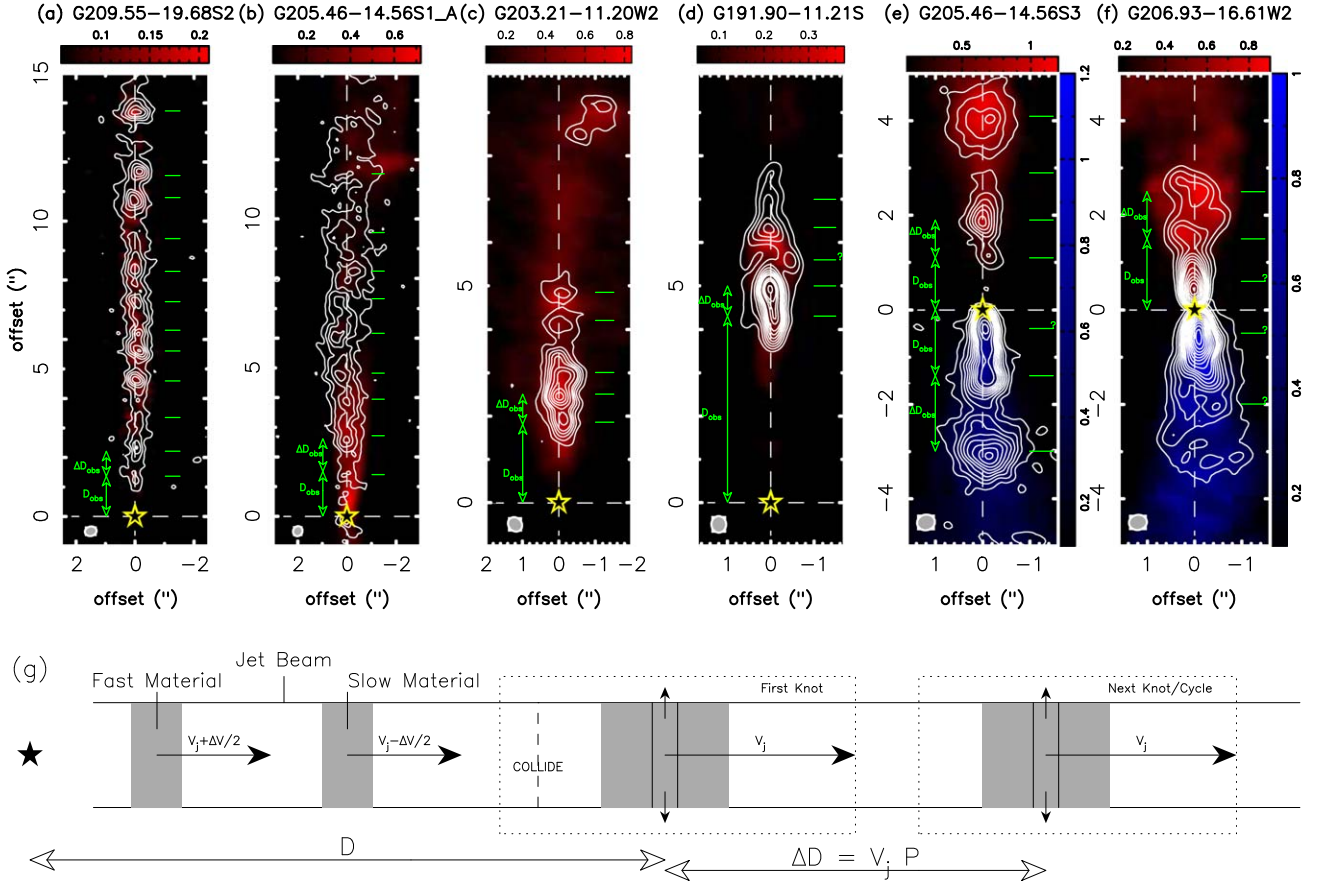
Figure 1. Panels (a) to (f): CO (red color for redshifted and blue color for blueshifted) intensity maps and SiO (white contour) intensity maps for the six ALMASOP sources, G209 (HOPS 10), G205 (HOPS 358), G203, G191, G205S3 (HOPS 315), and G206 (HOPS 399). These maps have been rotated clockwise by 29°, 158°, 146.7°, −5°, −135°, and −20°, respectively, to align the jets with the vertical axis. For SiO, the contour levels start at 3σ with a step of 3σ, and σ are ∼0.02, 0.04, 0.01, 0.02, 0.03, and 0.06 Jy beam⁻¹ km s⁻¹ in panels (a) to (f), respectively. The green line segments indicate the SiO peak positions of the knots. The yellow-black stars denote the central source position. The green arrows mark the lengths of $D_{\rm obs}$ and $\Delta D_{\rm obs}$. Panel (g): Schematic diagram showing how fast and slow jet material interact to form the internal shocks seen as knots (Raga et al. 1990; Stone & Norman 1993; Suttner et al. 1997; Lee & Sahai 2004; Jhan & Lee 2016).

radial jet velocity ($V_{\rm obs}$) are, respectively, given by

$$\Delta V_{\rm obs} = \Delta V \cos i, \qquad (5)$$

$$V_{\rm obs} = V_{\rm j} \sin i, \qquad (6)$$

where i is the inclination angle of the jet to the plane of the sky. With Equations (4) and (5), we have

$$V_{\rm j} \cos i = \pi \frac{D}{\Delta D} \Delta V_{\rm obs} = \pi \frac{D_{\rm obs}}{\Delta D_{\rm obs}} \Delta V_{\rm obs}, \qquad (7)$$

where $D_{\rm obs}$ is the observed (projected to the plane of the sky) distance from the sources to their first knots and $\Delta D_{\rm obs}$ is the observed (projected to the plane of the sky) average interval of the knots. Here, $D/\Delta D$ is equal to $D_{\rm obs}\Delta/D_{\rm obs}$ because of the same projection effect. Then, from Equations (6) and (7), we can derive the inclination angle with the following:

$$i = \tan^{-1}\left(\frac{V_{\rm j} \sin i}{V_{\rm j} \cos i} \right) = \tan^{-1}\left(\frac{V_{\rm obs}}{\pi \frac{D_{\rm obs}}{\Delta D_{\rm obs}} \Delta V_{\rm obs}} \right). \qquad (8)$$

using the values measured from the observations, and then V_j with Equation (6).

Table 1 shows the values of $D_{\rm obs}$ and $\Delta D_{\rm obs}$ measured from the total intensity SiO maps (Figure 1), the values of $\Delta V_{\rm obs}$ and $V_{\rm obs}$ measured from the SiO PV diagrams (Figure B1 in

Appendix B and Figure 1 in Dutta et al. 2022), and the corresponding values of i, $V_{\rm j}$, and thus P derived from the shock-forming model. Here the distance where the shock first forms $D_{\rm obs}$ is uncertain and is thus assumed to have an error of $0.5\Delta D_{\rm obs}$ on the negative side and half of the beam size on the positive side, where $\Delta D_{\rm obs}$ is the mean separation between the two consecutive knots. Notice that the first knots on the blueshifted side of G205S3 and on the both sides of G206 are too close to the sources to form shocks and thus should have a different origin. Therefore, we adopted the knots downstream to be the first knots formed by shocks.

3.2. CO Outflows and the Wide-angle Wind-driven Shell Model

CO outflows are detected in blue- and redshifted lobes for all the sources. Here we present the CO outflow maps for four of them (Figure 2), because the CO outflows of G205S3 and G206 have been reported and analyzed before (Figures 2 (a) and (c) in Dutta et al. 2022). The outflows display shell-like structures around the jets. Due to the projection effect, the structure of the outflow shells is better seen at low velocities close to the systemic velocity; thus, we present only one or two velocity channels close to $V_{\rm sys}$ to show the outflow shell structures. As can be seen, these outflow shells have larger opening angles and thus less collimation than their associated SiO jets.

Table 1
Quantities Measured from the SiO Jets and the Derived Quantities from the Shock-forming Model

Source Name	D_{obs} ($''$)	ΔD_{obs} ($''$)	ΔV_{obs} (km s^{-1})	V_{obs} (km s^{-1})	i ($°$)	V_j (km s^{-1})	P (yr)	Reference
G209 (HOPS 10)	$1.3^{+0.2}_{-0.4}$	0.8 ± 0.2	20	49	$28^{+0.7}_{-0.6}$	104^{+25}_{-20}	17	
G205 (HOPS 358)	$1.4^{+0.2}_{-0.5}$	1.0 ± 0.2	20	1.6	$1.0^{+0.6}_{-0.2}$	88^{+12}_{-20}	22	
G203	$1.8^{+0.2}_{-0.5}$	1.0 ± 0.2	20	30.8	18^{+4}_{-5}	117^{+12}_{-30}	17	
G191	$4.1^{+0.2}_{-0.45}$	0.9 ± 0.2	20	8.9	$1.8^{+0.2}_{-0.2}$	286^{+14}_{-30}	6	
G205S3 (HOPS 315) redshifted	$1.1^{+0.2}_{-0.55}$	1.1 ± 0.2	20	70	48^{+13}_{-5}	94^{+8}_{-18}	33	
G205S3 (HOPS 315) blueshifted	$1.5^{+0.2}_{-0.75}$	1.5 ± 0.2	20	80	52^{+16}_{-4}	102^{+5}_{-17}	45	
G206 (HOPS 399) redshifted	$1.5^{+0.2}_{-0.5}$	1 ± 0.2	40	50	15^{+6}_{-2}	195^{+20}_{-60}	16	
HH 211	$2.4^{+0.5}_{-1}$	2 ± 0.5	30	20	$10^{+6}_{-1.7}$	114^{+24}_{-46}	27	1
HH 211-obs[a]	2.6	2	30	20	11 ± 1	104 ± 16		1
HH 212	$4.5^{+0.5}_{-1}$	2 ± 0.5	20	7.3	$3^{+0.7}_{-0.3}$	141^{+16}_{-30}	27	2
HH 212-obs[a]					4 ± 2	115 ± 50		2
L1448C(N) redshifted	$2.63^{+0.3}_{-1.1}$	2.2 ± 0.3	20	54	$36^{+0.7}_{-3}$	92^{+7}_{-2}	40	3
L1448C(N) blueshifted	$1.87^{+0.3}_{-1.6}$	3.2 ± 0.3	20	61.2	59^{+30}_{-7}	71^{+6}_{-10}	122	3
L1448C(N)-obs[a]					40 ± 6	88 ± 10		3

Note.
[a] From proper-motion measurements and their radial velocity.
References: (1) Jhan & Lee (2016, 2021); (2) Zinnecker et al. (1998), Lee et al. (2015, 2017); (3) Hirano et al. (2010), Yoshida et al. (2021).

As discussed in Lee et al. (2000) and Dutta et al. (2022), a wide-angle wind-driven shell model can be used to fit the outflow shells and obtain their inclination angle, opening angle, and dynamical age. This model will thus be used to derive the inclination angle of the outflows to be compared with that of the jets derived earlier. In this model, the outflow shell is assumed to be a radially expanding parabolic shell with its structure and velocity given in the cylindrical coordinate system (z, R) by

$$z = cR^2 \qquad (9)$$

$$v_R = \frac{R}{t_0}, \qquad (10)$$

where c is a free parameter negatively correlated with the opening angle of the shell structure and t_0 is the dynamical age of the outflow shell to be obtained. The resulting shell structure projected on the sky (x', z'; as horizontal axis and vertical axis in Figures 2(a) to (d)) and the PV structure along the jet axis (v_{obs}, z'; as horizontal axis and vertical axis in Figures 2(e) to (h)) would be

$$z' = cx'^2 \cos i \left(1 - \frac{\tan^2 i}{4c^2 x'^2}\right) \qquad (11)$$

and

$$z' = -\frac{v_{obs} t_0}{\tan i} - \frac{1}{2c \tan i \sin i}\left[-1 \pm \sqrt{1 - \frac{4c v_{obs} t_0 \tan i}{\cos i}}\right], \qquad (12)$$

respectively, where i is the inclination angle. From Equation (11), we can see that the model produces a parabolic shell with its opening angle mainly depending on c. This parabolic shell corresponds to the boundary of the observed outflows in the low-velocity channel maps (Figures 2(a) to (d)). Based on Equation (12), this model produces a tilted parabolic PV structure with its tilt and opening angle depending on i, c, and t_0. Therefore, for each outflow, we have obtained the values of i, c, and t_0 (see Table 2) by fitting Equation (11) to the boundary of the outflow in the low-velocity channel maps (Figures 2(a) to (d)), and by searching the tilted parabolic PV structure and then fitting Equation (12) to its tilt and opening angle in the PV diagrams (Figures 2(e) to (h)). Note that the values for G205S3 and G206 are taken from Dutta et al. (2022). The errors of these parameters are estimated from the uncertainty of the intensity peak values in the observed channel maps and PV diagrams (Figure 2).
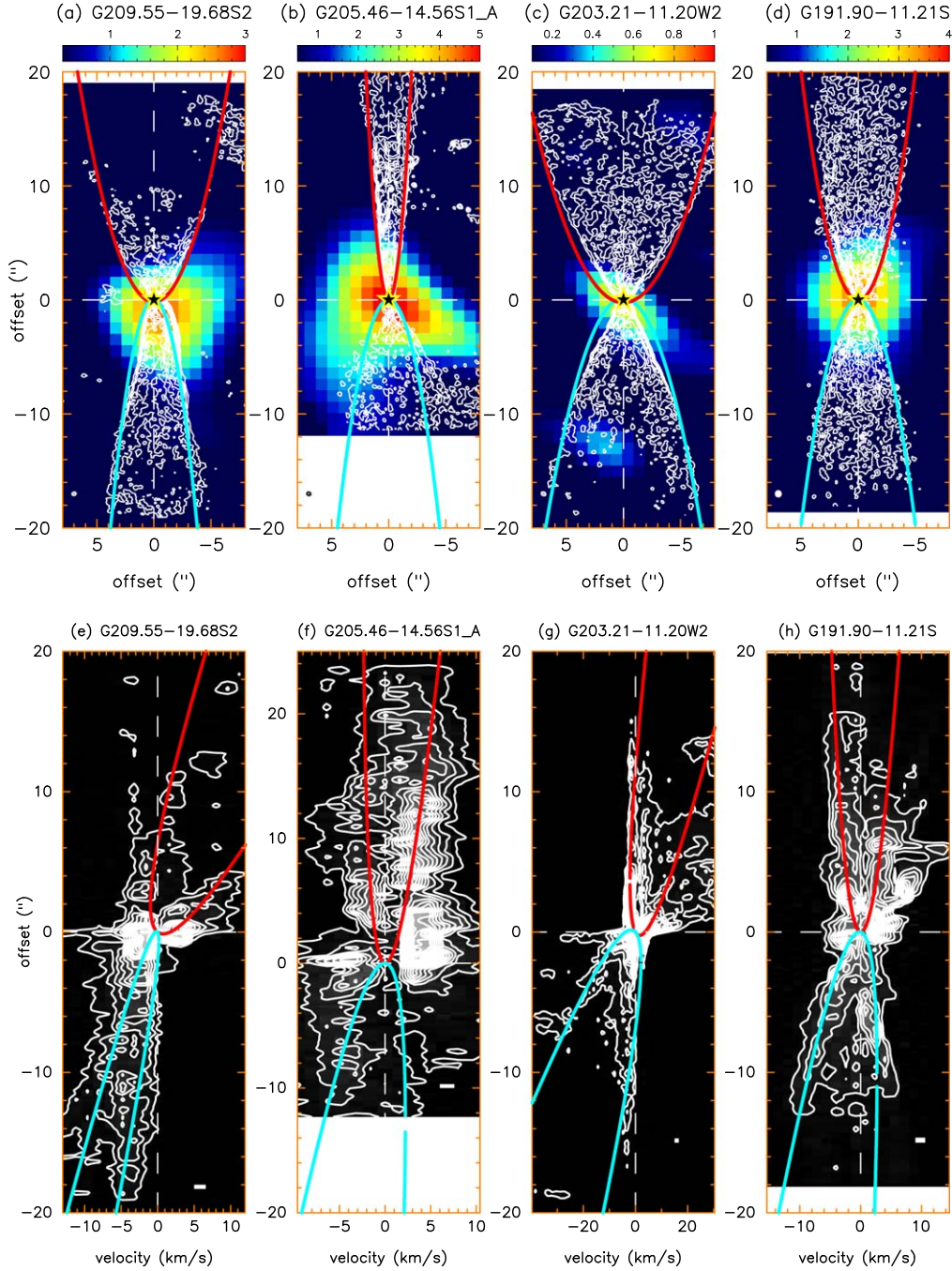
Figure 2. Panels (a) to (d): CO channel maps (contours) and $C^{18}O$ total intensity maps (color image) for the four ALMASOP sources G209 (HOPS 10), G205 (HOPS 358), G203, and G191. The contour levels start at 3σ with a step of 3σ, and the σ are $\sim$0.013, 0.016, 0.013 and 0.016 Jy beam^{-1} km s^{-1} in panels (a) to (d), respectively. The yellow-black stars denote the central source position. Panels (e) to (h): CO PV diagrams cut along the outflow axis for the four sources. The contour levels start at 10σ with a step of 10σ, and σ are $\sim$0.002, 0.0012, 0.001, and 0.002 Jy beam^{-1} in panels (e) to (h), respectively. The blue and red curves are the fits to the structures and PV structures of the outflows from the wind-driven shell model (see Section 3.2).

4. Discussion

As can be seen from Table 2, the inclination angles derived for the jets, i(SiO), using the shock-forming model are broadly consistent (within the errors) with those derived for the associated outflows, i(CO), using the wind-driven shell model. The inclination angles of the jet and the outflow are expected to be roughly the same because the jet and the underlying wind (that drives the outflow) are believed to come from the same accretion disk. Thus, this consistency supports that the shock-

forming model can be used to derive the inclination angle and velocity of the jets. Notice that, in order for this model to work, the jets must have at least a few roughly equally spaced knots produced by internal shocks. In addition, the shock speed (ΔV) should be around 10–40 km s^{-1} (Schilke et al. 1997) so that the SiO emission is indeed produced by shocks. Moreover, no significant energy is dissipated in the shocks so that the thermal energy produced by the shocks can be totally transferred sideways into the sideways ejection.

Table 2
Inclination Angle of the SiO Jets and the Derived Quantities of the CO Outflows from the Wide-angle Wind-driven Shell Model

Source Name	HOPS	i (SiO) (°)	i (CO) (°)	c (arcsec^{-1})	t_0 (km s^{-1} arcsec^{-1})
G209 Red	HOPS 10	$28^{+0.7}_{-0.6}$	30 ± 5	0.55 ± 0.05	0.7 ± 0.1
G209 Blue	HOPS 10		30 ± 3	1.6 ± 0.3	1.3 ± 0.2
G205 Red	HOPS 358	$1.0^{+0.6}_{-0.2}$	5 ± 2	1 ± 0.3	1.2 ± 0.3
G205 Blue	HOPS 358		4 ± 1	4 ± 1	0.4 ± 0.15
G203 Red		18^{+4}_{-5}	30 ± 3	0.3 ± 0.1	0.6 ± 0.2
G203 Blue			30 ± 4	0.5 ± 0.1	0.35 ± 0.05
G191 Red		$1.8^{+0.2}_{-0.2}$	2 ± 0.5	0.8 ± 0.2	0.9 ± 0.2
G191 Blue			10 ± 2	0.8 ± 0.1	0.65 ± 0.1
G205S3 Red	HOPS 315	48^{+13}_{-5}	40 ± 8[a]	0.26[a]	
G205S3 Blue	HOPS 315	52^{+16}_{-4}	40 ± 8[a]	0.2[a]	
G206 Red	HOPS 399	15^{+6}_{-2}	10 ± 5[a]	0.8[a]	

Note.
[a] Reference: Dutta et al. (2022).

4.1. Application to Other Sources

In order to further test the shock-forming model, we applied it to three previously reported SiO jets, HH 211 (Jhan & Lee 2016, 2021), HH 212 (Lee et al. 2015), and L1448C(N) (Yoshida et al. 2021), of which the jet velocity and inclination angle have been derived independently from proper-motion measurements and the observed radial velocity. In the case of HH 211, the first pair of knots (knots BK0 and RK0) are too close (<25 au) to the source, so they are unlikely formed by shocks and thus excluded from our analysis. In the case of HH 212, we also included the H$_2$ knots in our analysis (see Figures 4 and 6 in Lee et al. 2015) because the shocks there are too strong for SiO to survive and thus are only seen in H$_2$. In the case of L1448C(N), the first pair of knots (R1-a and Bl-a) is seen with a large velocity range of >40 km s^{-1}, which is too large a shock velocity for SiO to survive (Schilke et al. 1997; May et al. 2000; Gusdorf et al. 2008; Van Loo et al. 2013). Also, their PV structures are not fully resolved and thus might have a different origin. Therefore, the first pair of knots in this jet are excluded from our analysis. As can be seen in Table 1, the derived inclination angle and velocity of the jet in these three jets are also broadly consistent with those previously measured from proper motion and radial velocity.

4.2. Jets and Outflows

In our sample, four of the jets detected in SiO are monopolar and are seen only on the redshifted side, although their associated CO outflows are bipolar. As mentioned earlier, the same jets are also detected in CO and also appear to be monopolar on the redshifted side. This asymmetry of the jets is unlikely to be caused by an asymmetry of the ambient material, which can only affect material at low velocity in the CO outflow (Codella et al. 2014). In fact, a monopolar jet has also been detected in SiO in NGC 1333IRAS2A, although on the blueshifted side (Codella et al. 2014). Because dust extinction is negligible in radio wavelengths, the lack of a redshifted jet

component in that system is likely intrinsic. Thus, the authors argued that the accreting disk in that system is ejecting more material from the side tilted toward us than from the side tilted away from us, producing the blueshifted monopolar jet. This scenario can also apply to our jets, but with the accreting disks ejecting more material from the side tilted away from us.

The CO outflows also show asymmetry in intensity maps and PV diagrams (Figure 2), with different opening angles on each side of the source (column 5 in Table 2). It could be due to an accumulative interaction of the jet and wind with the ambient material within their dynamical age, which is ~2000 years (column 6 in Table 2). Some asymmetry is seen in the ambient material in the C^{18}O total intensity maps around the sources (Figures 2(a) to (d)); however, further observations at a larger scale are needed to check it.

In our shock-forming model, the SiO knots in the jets are produced by a periodic variation in the jet velocity. The SiO PV structure along the jet axis (Figure B1) also indicates the presence of variation in the jet velocity, with the fast jet material catching up with the slow jet material. The reason for such a variation is not clear, and it may be caused by the orbital motion of a binary companion (Machida et al. 2008), semiperiodic variation of the jet-launching radius (Shu et al. 2000; Pudritz et al. 2007), or the variation of magnetic field morphology in the star–disk system (Frank et al. 2014), etc. Alternatively, the knots could be due to periodic enhanced mass ejections. However, it is unclear how such ejections can form shocks (Frank et al. 2014) to produce the observed SiO knotty shocks.

4.3. Jet Knot Timescales and Mid-IR/Submillimeter Light-curve Variability

It is striking that the majority of jets analyzed in this paper have knot timescales on the order of decades (Table 1), suggesting that there is some recurrent form of disk or accretion instability operating at this frequency. It is therefore useful to compare these jet knot results against long-term, many-year

monitoring observations of the mid-IR and submillimeter continuum emission from similar young stellar objects across the Gould Belt.

Park et al. (2021) analyzed 7 yr mid-IR light curves of 735 protostars, classifying 140 (20%) as having dominant brightness variation timescales longer than three years. Similarly, Lee et al. (2021) classified 4 yr submillimeter light curves of 43 protostars and recovered 15 (35%) with dominant periods longer than three years. In both cases, the majority of these light-curve variations are longer than the observing window while also showing evidence of curvature, suggesting dominant timescales of decades. Furthermore, the estimated amplitude variations imply order-unity changes in the central source luminosity, attributed to order-unity variability in the protostellar mass accretion rate (Johnstone et al. 2013). For sources common to both investigations, the mid-IR and submillimeter light curves of the long-term variables show strong similarities (Contreras Pena et al. 2020; Lee et al. 2021).

Three of the nine sources investigated in this paper are monitored in the submillimeter (G205S1, G205S3, and HH 211), and all show long-term variability. A further three sources were included in the mid-IR sample (G205S3, G209S2, and L144CN) with only L1448C(N) showing definite long-term variability. Separately, Dutta et al. (2022) reports that G206W2 is undergoing a long-term mid-IR secular change. We have checked the mid-IR light curves (NEOWISE; Cutri et al. 2015) for the other five sources by eye. G191S, G205S1, and HH 212 are definite long-term variables. In summary, a clear majority of this paper's jet knot sources show evidence of many-year accretion variability.

5. Conclusions

We have studied the jets and outflows in six sources and mapped them in SiO ($J = 5-4$) and CO ($J = 2-1$) at high resolution with ALMA. The jets consist of a chain of roughly equally spaced SiO knots that can be produced by semiperiodic variations in jet velocity. Thus, we have used a shock-forming model with a periodic variation in jet velocity to estimate the inclination angle and velocity of the SiO jets in these six sources from their SiO knots. We have also used a wide-angle wind-driven shell model to fit the shell structure and PV diagrams of the CO outflows to derive the inclination angles of the CO outflows. The derived inclination angles of the SiO jets and CO outflows are broadly consistent with each other. We also applied the shock-forming model to three additional SiO jets reported in the literature and found that the derived jet velocity and inclination angle are also broadly consistent with those previously estimated from proper motion and radial velocity. Our results support that the knots in the jets are indeed produced by semiperiodic variations in jet velocity, so that the shock-forming model can be used to determine the velocity and inclination angle of the jets from the SiO knots. The periods of the velocity variations are on the order of decades for most of the jets studied here.

Appendix A
C^{18}O PV Structure Used to Derive the Systemic Velocity

Figure A1 shows the C^{18}O PV diagrams for the four ALMASOP sources (G209, G205, G203, and G191). The vertical dash line indicates the systemic velocity for each source, which are used in Section 3.
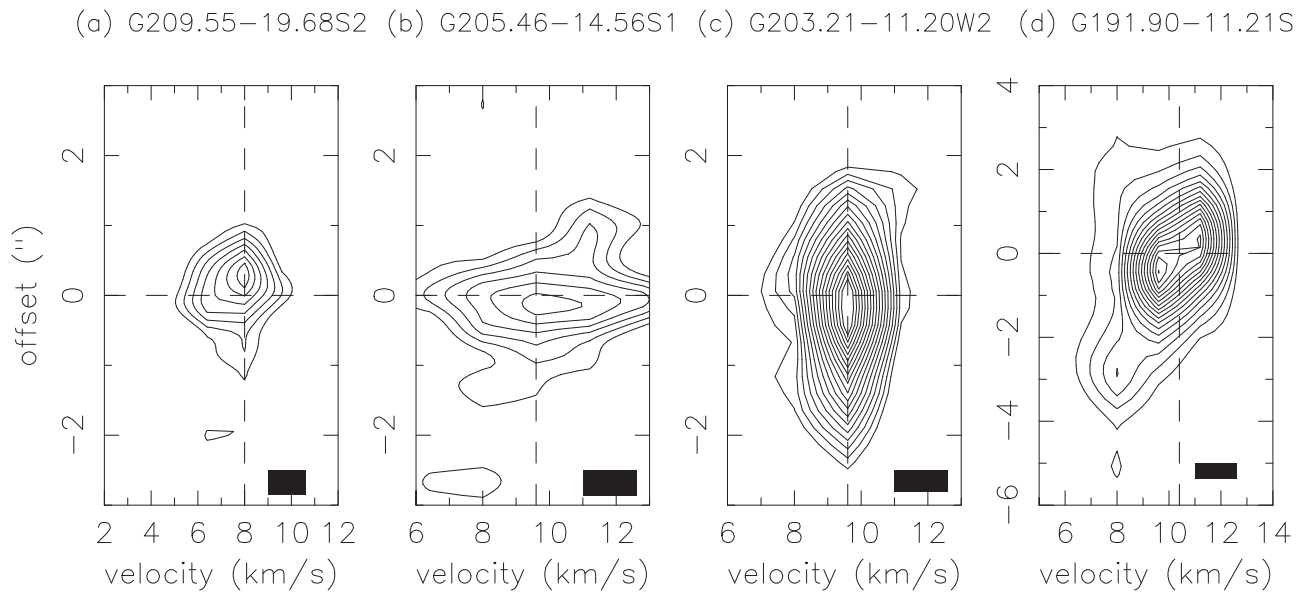
(a) G209.55−19.68S2 (b) G205.46−14.56S1 (c) G203.21−11.20W2 (d) G191.90−11.21S

Figure A1. PV diagrams cut perpendicular to the jet axis going through the sources' center for four sources (G209, G205, G203, and G191) in C^{18}O, centered at the source position. The contour levels start at 3σ with a step of 3σ, and σ are ∼0.003, 0.003, 0.003, and 0.003 Jy beam^{-1} in panels (a) to (d), respectively. The vertical dashed line indicates the systemic velocity for each source.

Appendix B
SiO PV Structure along the Jet Axis

Figure B1 shows the PV diagrams of the jets along the jet axis in SiO. The width of the green line segment denotes the

observed radial sideways-ejection velocity (δV_{obs} in Equation 5) for each source, and the dotted line denotes the observed radial jet velocity (V_{obs} in Equation 6).
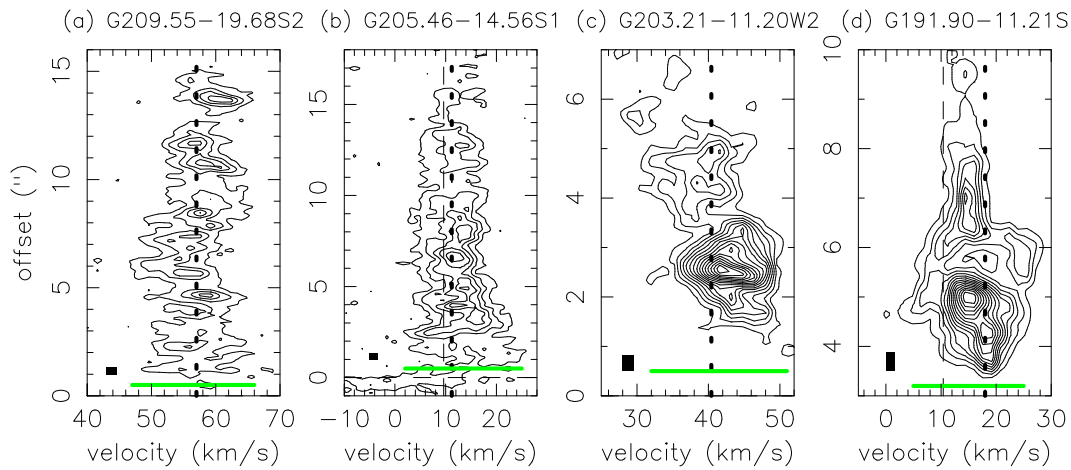
Figure B1. PV diagrams of the jets along the jet axis in SiO. The width of the green line segment denotes the observed radial sideways-ejection velocity (ΔV_{obs}) for each source, and the dotted line denotes the observed radial jet velocity (V_{obs}). The contour levels start at 3σ with a step of 3σ, and σ are ~0.002, 0.002, 0.002, and 0.0019 Jy beam^{-1} in panels (a) to (d), respectively.

ORCID iDs

Kai-Syun Jhan ● https://orcid.org/0000-0003-2069-1403
Chin-Fei Lee ● https://orcid.org/0000-0002-3024-5864
Doug Johnstone ● https://orcid.org/0000-0002-6773-459X
Tie Liu ● https://orcid.org/0000-0002-5286-2564
Sheng-Yuan Liu ● https://orcid.org/0000-0003-4603-7119
Naomi Hirano ● https://orcid.org/0000-0001-9304-7884
Ken'ichi Tatematsu ● https://orcid.org/0000-0002-8149-8546
Somnath Dutta ● https://orcid.org/0000-0002-2338-4583
Hsien Shang ● https://orcid.org/0000-0001-8385-9838
Jeong-Eun Lee ● https://orcid.org/0000-0003-3119-2087
Shanghuo Li ● https://orcid.org/0000-0003-1275-5251
Chun-Fan Liu ● https://orcid.org/0000-0002-1624-6545
Shih-Ying Hsu ● https://orcid.org/0000-0002-1369-1563
Woojin Kwon ● https://orcid.org/0000-0003-4022-4132
Dipen Sahu ● https://orcid.org/0000-0002-4393-3463
Kee-Tae Kim ● https://orcid.org/0000-0003-2412-7092
Sheng-Li Qin ● https://orcid.org/0000-0003-2302-0613
Patricio Sanhueza ● https://orcid.org/0000-0002-7125-7685
Leonardo Bronfman ● https://orcid.org/0000-0002-9574-8454
Zhang Qizhou ● https://orcid.org/0000-0003-2384-6589
David Eden ● https://orcid.org/0000-0002-5881-3229
Alessio Traficante ● https://orcid.org/0000-0003-1665-6402
Chang Won Lee ● https://orcid.org/0000-0002-3179-6334

References

Codella, C., Cabrit, S., Gueth, F., et al. 2007, A&A, 462, L53
Codella, C., Maury, A. J., Gueth, F., et al. 2014, A&A, 563, L3
Contreras Pena, C., Johnstone, D., Baek, G., et al. 2020, MNRAS, 495, 3614
Cutri, R. M., Mainzer, A., Conrow, T., et al. 2015, Explanatory Supplement to the NEOWISE Data Release Products, Technical Report, Caltech, http://wise2.ipac.caltech.edu/docs/release/neowise/expsup
Dutta, S., Lee, C.-F., Johnstone, D., et al. 2022, ApJ, 925, 11
Dutta, S., Lee, C.-F., Liu, T., et al. 2020, ApJS, 251, 20
Frank, A., Ray, T. P., Cabrit, S., et al. 2014, in Protostars and Planets VI, ed. H. Beuther et al. (Tucson, AZ: Univ. Arizona Press), 451
Gueth, F., Guilloteau, S., & Bachiller, R. 1998, A&A, 333, 287
Gusdorf, A., Cabrit, S., Flower, D. R., et al. 2008, A&A, 482, 809
Herczeg, G. J., Johnstone, D., Mairs, S., et al. 2017, ApJ, 849, 43
Hirano, N., Ho, P. P. T., Liu, S.-Y., et al. 2010, ApJ, 717, 58
Hirano, N., Liu, S.-Y., Shang, H., et al. 2006, ApJL, 636, L141
Hsu, S.-Y., Liu, S.-Y., Liu, T., et al. 2020, ApJ, 898, 107
Jhan, K.-S., & Lee, C.-F. 2016, ApJ, 816, 32
Jhan, K.-S., & Lee, C.-F. 2021, ApJ, 909, 11
Johnstone, D., Hendricks, B., Herczeg, G. J., & Bruderer, S. 2013, ApJ, 765, 133
Lee, C.-F. 2020, A&ARv, 28, 1
Lee, C.-F., Hasegawa, T. I., Hirano, N., et al. 2010, ApJ, 713, 731
Lee, C.-F., Hirano, N., Zhang, Q., et al. 2015, ApJ, 805, 186
Lee, C.-F., Ho, P. T. P., Hirano, N., et al. 2007, ApJ, 659, 499
Lee, C.-F., Ho, P. T. P., Li, Z.-Y., et al. 2017, NatAs, 1, 0152
Lee, C.-F., Mundy, L. G., Reipurth, B., et al. 2000, ApJ, 542, 925
Lee, C.-F., & Sahai, R. 2004, ApJ, 606, 483
Lee, C.-F., Stone, J. M., Ostriker, E. C., et al. 2001, ApJ, 557, 429
Lee, Y.-H., Johnstone, D., Lee, J.-E., et al. 2021, ApJ, 920, 119
Machida, M. N., Inutsuka, S. I., Matsumoto, T., et al. 2008, ApJ, 676, 1088
May, P. W., Pineau des Forêts, G., Flower, D. R., et al. 2000, MNRAS, 318, 809
McCaughrean, M. J., Rayner, J. T., & Zinnecker, H. 1994, ApJL, 436, L189
Palau, A., Ho, P. T. P., Zhang, Q., et al. 2006, ApJL, 636, L137
Park, W., Lee, J.-E., Contreras Pena, C., et al. 2021, ApJ, 920, 132
Podio, L., Tabone, B., Codella, C., et al. 2021, A&A, 648, A45
Pudritz, R. E., Ouyed, R., Fendt, C., et al. 2007, in Protostars and Planets V, ed. B. Reipurth, D. Jewitt, & K. Keil (Tucson, AZ: Univ. Arizona Press), 277
Raga, A. C., Canto, J., Binette, L., et al. 1990, ApJ, 364, 601
Sahu, D., Liu, S.-Y., Liu, T., et al. 2021, ApJL, 907, L15
Schilke, P., Walmsley, C. M., Pineau des Forets, G., et al. 1997, A&A, 321, 293
Shu, F. H., Najita, J. R., Shang, H., et al. 2000, in Protostars and Planets IV, ed. V. Mannings, A. P. Boss, & S. S. Russell (Tucson, AZ: Univ. Arizona Press), 789
Stone, J. M., & Norman, M. L. 1993, ApJ, 413, 210
Suttner, G., Smith, M. D., Yorke, H. W., et al. 1997, A&A, 318, 595
Van Loo, S., Ashmore, I., Caselli, P., et al. 2013, MNRAS, 428, 381
Yoshida, T., Hsieh, T.-H., Hirano, N., et al. 2021, ApJ, 906, 112
Zinnecker, H., McCaughrean, M. J., & Rayner, J. T. 1998, Natur, 394, 862